Quasi-Neutral Modeling of Gliding Arc Plasmas

Stanimir Kolev,* Surong Sun, Georgi Trenchev, Weizong Wang, Haixing Wang, Annemie Bogaerts

The modelling of a gliding arc discharge (GAD) is studied by means of the quasineutral (QN) plasma modelling approach. The model is first evaluated for reliability and proper description of a gliding arc discharge at atmospheric pressure, by comparing with a more elaborate non-quasineutral (NQN) plasma model in two different geometries – a 2D axisymmetric and a Cartesian geometry. The NQN model is considered as a reference, since it provides a continuous self-consistent plasma description, including the near electrode regions. In general, the results of the QN model agree very well with those obtained from the NQN model. The small differences between both models are attributed to the approximations in the derivation of the QN model. The use of the QN model provides a substantial reduction of the computation time compared to the NQN model, which is crucial for the development of more complex models in three dimensions or with complicated chemistries. The latter is illustrated for (i) a reverse vortex flow (RVF) GAD in argon, and (ii) a GAD in CO_2. The RVF discharge is modelled in three dimensions and the effect of the turbulent heat transport on the plasma and gas characteristics is discussed. The GAD model in CO_2 is in a 1D geometry with axial symmetry and provides results for the time evolution of the electron, gas and vibrational temperature of CO_2, as well as for the molar fractions of the different species.

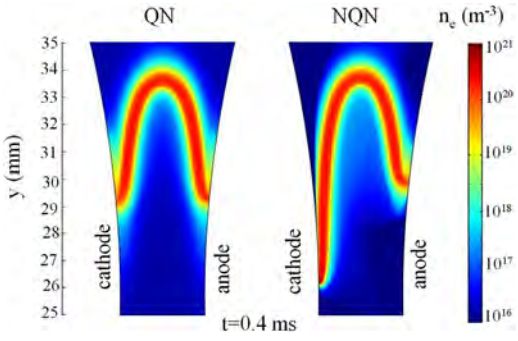

1. Introduction

A classical gliding arc discharge (GAD) is usually produced between two or more diverging electrodes placed in a fast gas flow at atmospheric pressure or higher.[1–3] The discharge starts at the shortest interelectrode distance and spreads out by gliding progressively along the electrodes in the direction of the flow, until it disappears after a certain time. Subsequently, a new discharge immediately starts again at the shortest interelectrode distance. More complicated GAD configurations also exist, combining a different discharge geometry with complex gas flow, like for example the reverse vortex flow (RVF) GAD,[3,4] or combining the discharge with an external magnetic field.[5] GADs are widely applied for pollution control,[6,7] CO_2 conversion,[4,8–11] surface treatment[12] and combustion enhancement,[13] due to their ability to simultaneously remain at highly non-equilibrium

St. Kolev
Faculty of Physics, Sofia University, 5 James Bourchier Boulevard, 1164 Sofia, Bulgaria
E-mail: skolev@phys.uni-sofia.bg
S.R. Sun, G. Trenchev, W. Wang, A. Bogaerts
Department of Chemistry, Research Group PLASMANT, University of Antwerp, Universiteitsplein 1, B-2610 Antwerp, Belgium
S.R. Sun, H. X. Wang
School of Astronautics, Beihang University, 100191 Beijing, China

conditions, while being characterized by a considerable electron temperature and electron density.

In recent years, GADs attract increasing interest worldwide because of the above-described interesting characteristics and thus, their importance in various applications. A considerable number of experiments have been conducted to study the slip velocity and column length,[14] the dynamic behavior,[15] and the electrical characterization.[16] Apart from the experimental studies, several theoretical studies have also been performed.[1,17–27] They are motivated by the need of a more profound understanding of the discharge operation, which is very difficult to be achieved with experimental methods, due to the complexity of the discharge – non-stationary behavior, complex plasma, etc. However, modelling a GAD is neither an easy task. There are several key properties, which make the modelling quite difficult. (i) The discharge has an intrinsically non-stationary and usually non-repetitive nature. Thus one needs to follow the whole discharge evolution (for a single period), in order to be able to derive the averaged (overall) effect on the underlying gas (mixture). This usually results in simulations with long computation time. (ii) The discharge ignition and re-ignition is determined by streamer (or ionization wave) propagation,[28] which is an extremely fast (nanoseconds) and hard to model phenomenon. (iii) The discharge is usually ignited in a forced gas flow, which can have well established turbulent behavior. The interaction of the plasma column with the turbulent gas might lead to a very unstable arc, as can be deduced from electrical measurements in GADs.[29] (iv) The discharge interaction with the electrodes is usually related to the formation of cathode spots, which are relatively tiny structures (tens of micrometers) with extreme electric field, requiring very fine mesh discretization within the numerical model. (v) The discharge behavior/type is not well defined, even for a particular experiment. It has been shown both experimentally[30] and theoretically[24] that the discharge can behave as an arc or glow discharge, depending on the cathode local surface properties, and even within a single period, the discharge can change the regime, due to local variations in the cathode electron field emission capabilities.

All these complications of the discharge nature force researchers to make considerable simplifications in the numerical models, in order to make the discharge modelling possible and feasible. Therefore, having relatively limited computational resources, the early models of GADs are based on the relatively simplified gas energy balance, assuming an equilibrium plasma.[1,17,21] However, GADs are usually operating far from thermal equilibrium and this approach gives only a rough calculation of the discharge parameters. In[19] the treatment is extended to a non-equilibrium plasma, based on an analytical relation between the electric field and the electron and gas temperature. Some of the studies also focus only on the calculation of the discharge electrical parameters[20] or only consider a 0D model in the case of a complex chemistry.[22]

In the last few years, some new research efforts were initiated on GAD modelling, with the ambitious aim to provide a better fundamental understanding of the discharge behavior and to evaluate the discharge characteristics with respect to the conversion of CO_2 in a GAD. Several works have been published already.[23–27] The first comprehensive model was developed in,[23] with special focus on the arc-electrodes interaction and the ''gliding'' along the electrodes. In,[24,26] the difference between arc and glow discharge regime was studied, and in,[25,27] the configuration of a reverse vortex flow GAD was studied.[3,4] In[31] a discharge in CO_2 is considered and the plasma parameters and CO_2 conversion rate inside the arc column are obtained. Despite the increased computational power of modern PCs, the complexity of GADs still enforces some simplifications to be made in the models. For example considering 2D models,[23,24] in[31] a 1D model is presented because of the complex CO_2 chemistry, while[25] is a full three-dimensional model but with very simplified chemistry.

The models presented in this work, are based on the fluid approach of plasma modelling, derived as the moment equations of the electron energy distribution function from the electron Boltzmann equation.[32,33] We will use these equations without presenting their derivation here, since they are well known from basic plasma physics books.[32,33] Usually the equations of mass, momentum and energy conservation are coupled with the Maxwell equations in order to derive the plasma behavior. If the magnetic field does not play an important role and the time variation of the field is slow enough, one could consider an electrostatic model by coupling the conservation equations with either the Poisson or the current conservation equation. In,[23,24] the conservation equations are coupled with the Poisson equation and these models describe the whole discharge structure, including the near wall (electrode) regions, i.e., the sheaths, which are characterized with strong nonuniformity and deviation from quasineutrality. However, the numerical cost of such models is extremely high when applied to a three-dimensional GAD or even to lower dimensional GAD configurations with complex chemistry. Our motivation for the study of GADs is tightly related to CO_2 decomposition in plasma and this application is characterized by very complex plasma chemistry, including the vibrational kinetics,[34,35] and in some cases also with a complex geometry with specific gas flow patterns.[4,13,25] Thus, considerable simplifications need to be applied, compared to the coupled solution of the conservation equations with

the Poisson equation, in order to make the numerical simulation of complex GADs feasible. In this work we present the simplification path we have undertaken, together with a comparison with the more elaborate models from.[23,24]

Different alternatives for the model simplification and the reduction of the computation cost/time have been considered. It was concluded that for the considered conditions, a quasineutral (QN) model could provide a significant reduction in the computation time, while preserving the model accuracy for the main part of the discharge. In,[24] we have shown that the arc body is actually unaltered, even when considering both arc and glow regime of the discharge operation, i.e., completely different properties of the near cathode region of the arc. The regime is determined mainly by the electrode surface properties and thus it could be very specific for every experiment. Taking this into account, in order to generalize the results obtained by modelling, it makes sense to describe only the plasma channel, which is less dependent on the electrode surface properties, as shown in.[24] Therefore the QN model developed here is a viable option because it describes only the discharge body, excluding the electrode sheath and thus it describes both the arc and glow regimes. In this paper, we will validate the QN model for the GAD, to clearly illustrate its advantages and limitations. For this purpose, we will show how the QN model compares with the more accurate non-quasineutral model (NQN) in 2D in the arc regime, but similar results can be obtained when considering the glow discharge regime, as shown in.[24] This allows us to evaluate the "price" that needs to be paid for the simplifications made in the QN model. Thus, this study presents an important milestone for the further evaluation and interpretation of the results obtained from GAD QN models of complex discharge configurations. Furthermore, the use of this approach is demonstrated with two models – a three-dimensional model of a reverse vortex flow GAD (also called plasmatron) in argon and a 1D model of a GAD operating in CO_2.[4,13,25]

It is worth to mention that the QN model has been widely used in plasma numerical simulations for many years, dating back to the mid-1980s, and some representative examples can be found in references,[36–39] but it is the first time that a QN model is used to study in detail a gliding arc.

The paper has the following structure. In section 2 the QN model developed for the GAD is described in detail, together with the comparison with the NQN model. Since the description of the NQN model was presented in our previous papers,[23,24] here we omit its detailed description. In section 3 we demonstrate the three-dimensional QN model for the case of a RVF GAD, and we analyze specifically the effect of turbulent heat and mass transport on the plasma column. In section 4 we present results from a 1D QN model in pure CO_2 and we show the time evolution of various temperatures and of the molar fractions of the main plasma species. Finally the conclusions are given in section 5.

2. Limitations and Reliability of a Quasineutral Plasma Model for Gliding Arc Discharge Modeling

In this section we show the properties and the limitations of the QN approach in the context of GADs.

2.1. Model Description

To properly account for the fundamental mechanisms in a GAD, which is inherently a three-dimensional system, we use a combination of two 2D geometries, i.e., a 2D Cartesian coordinate system and a 2D cylindrical coordinate system with axial symmetry (axisymmetric), similar to.[23,24]

The geometry considered in the Cartesian model is plotted in Figure 1(a). As explained in,[24] here we use a slightly reduced geometry compared to[23] in order to reduce the computation time, because we do not consider a whole cycle of the discharge gliding process. The geometry considered in the axisymmetric model is a simple cylinder and is plotted in Figure 1(b). In all models used in this section, we employ the same argon kinetic chemical reactions, presented in Tables 1 and 2 of reference.[23]

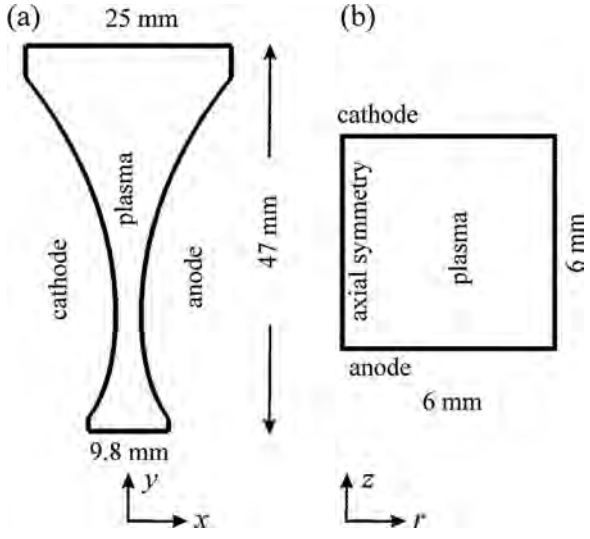

Figure 1. Geometries considered in the models: (a) 2D Cartesian and (b) 2D axisymmetric model.

2.1.1. NQN Cartesian Model

The NQN Cartesian model is the same as in.[23,24] It considers the particle balance equations for all species, the electron energy balance equation, the gas thermal balance, gas flow equations, and the Poisson equation. More details can be found in.[23,24]

2.1.2. NQN Axisymmetric Model

The NQN axisymmetric model is the same as in[24] and similar to.[23] The only difference compared to[23] is the addition of a loss term in all balance equations, accounting for the convective processes. For more details, we refer to[24] and to section 2.1.3 below.

2.1.3. QN Cartesian Model

Particle balance equations: The particle balance equations have the usual form:

$$\frac{\partial n_s}{\partial t} + \vec{\nabla} \cdot \vec{G}_s + (\vec{u}_g \cdot \vec{\nabla}) n_s = S_{c,s} \tag{1}$$

where n_s is the species density, G_s is the species flux in a reference frame moving with the gas velocity u_g, and $S_{c,s}$ is the collision term representing the net number of particles produced or lost in the volume reactions. Note that in the above equation the term $n_s(\vec{\nabla} \cdot \vec{u}_g)$ is neglected, since at normal conditions (without shock waves or similar phenomena) it is small. An often used approximation for the momentum conservation equation is the drift-diffusion approximation, in which the flux G_s (with respect to the gas velocity) is determined by drift due to the electric field and diffusion:

$$\vec{G}_s = \frac{q_s}{|q_s|} \mu_s n_s \vec{E} - \vec{\nabla} D_s n_s. \tag{2}$$

In this expression, D_s is the diffusion coefficient and μ_s is the mobility of the corresponding species "s", q_s is their charge, and $\vec{E}$ is the electric field. Equation 2 is used directly for the expression of the flux in Equation 1, and thus Equation 1 becomes a second order partial differential equation for n_s. If we assume quasineutrality (i.e., the number of negative species is equal to the number of positive species at any point in the domain)

$$n_e = n_{Ar^+} + n_{Ar_2^+} \tag{3}$$

we cannot use the Poisson equation for the derivation of the electric field generated by the plasma itself (the ambipolar field), since the charge density will always be zero. In this case, an alternative approach instead of the Poisson equation is to use the current continuity equation (Equation 10, to be discussed later) for the derivation of the electric field in the plasma,[40] i.e., coupling Equation 1 for all charged species with charge continuity for the electric field. This, however, requires proper boundary conditions at the interface between wall sheath and quasi-neutral plasma. Such boundary conditions are usually based on an analytical model of the plasma transport in the sheath. Such models are non-trivial and they become rather cumbersome for complex plasmas with many different charged species. In order to avoid unnecessary complications of the models, we have adopted further simplifications to the model, which – as will be shown later – do not harm the reliability of the obtained results for the considered conditions of an atmospheric pressure plasma.

Let us represent for convenience the electric field as the sum of an ambipolar field E_{amb} and a driving field E_d due to external sources. If both electric field components (E_{amb} and E_d) are in different directions, we can obtain E_{amb} by making one more approximation, namely for the equality of the fluxes of positive and negative species. In the current configuration with electrons and two types of positive ions (Ar^+ and Ar_2^+) we can write that

$$\vec{G}_e = \vec{G}_{Ar^+} + \vec{G}_{Ar_2^+} \tag{4}$$

or if we take into account Equation 2 we obtain

$$(\mu_{Ar_2^+} n_{Ar_2^+} + \mu_{Ar^+} n_{Ar^+}) \vec{E}_{amb} - D_{Ar_2^+} \vec{\nabla} n_{Ar_2^+} - D_{Ar^+} \vec{\nabla} n_{Ar^+}$$
$$= -\mu_e n_e \vec{E}_{amb} - D_e \vec{\nabla} n_e, \tag{5}$$

where we have ignored the thermo-diffusion, i.e., we assume that $D_s \vec{\nabla} n_s >> n_s \vec{\nabla} D_s$ for all species. Inserting Equation 3 in Equation 5 and following[41] and considering the two types of ions (Ar^+, Ar_2^+), we can express the ambipolar electric field as:

$$\vec{E}_{amb} = \frac{(D_{Ar^+} - D_e) \vec{\nabla} n_{Ar^+} + (D_{Ar_2^+} - D_e) \vec{\nabla} n_{Ar_2^+}}{(\mu_{Ar^+} + \mu_e) n_{Ar^+} + (\mu_{Ar_2^+} + \mu_e) n_{Ar_2^+}} \tag{6}$$

The ambipolar diffusion approximation is one of the basic approaches to the description of the positive column and dates back to the Schottky theory.[42] Later many researchers modified and developed the ambipolar diffusion theory.[43–45] Strictly speaking, the electron flux is equal to the ion flux (Equation 4) only in very specific conditions, like no direct influence of the external field on the ambipolar field, combined with discharge symmetry or steady state conditions and dielectric walls. Of course, this assumption is certainly an approximation in our case. This is exactly the reason why we need to validate our model. From the following comparisons, it can be seen that this approximation is reasonable and does not have much influence on the results. Certainly we can build a much more consistent QN model

without this equal flux assumption. However, in this case we need to use an appropriate boundary condition at the plasma-sheath transition near the electrodes and thus add one more balance equation in the model. As we can see from the following results, there is no profit of adding this extra complexity to the model, as the results of the current model are in excellent agreement with the full (NQN) model, and adding this complexity would again increase the calculation time.

As noted above, the derivation of Equation 6 is strictly correct only if the driving field does not have a component in the direction of the ambipolar field, i.e., both drifts due to the electric field are independent. In general this is not the case for GADs due to their complex shape. However, both numerical results (see for example in section 2.2.1 below) and experiments show that the arc is usually formed as a bended cylinder (string) as a result of discharge contraction.[15,29] Most of the current between the electrodes is flowing along the arc, and thus within the arc the driving field E_{d} is directed along the arc. On the other hand, the ambipolar field (Equation 6) is determined by the gradients of the densities, and since the gradients are mainly in the direction perpendicular to the arc, the calculated ambipolar field will be mainly in the direction perpendicular to the arc. Thus in the core parts of the arc (with highest density and currents) both fields (E_{amb} and E_{d}) remain perpendicular, which can explain why the approximation in the derivation of E_{amb} has only minor effect on the calculation results, and why it results in a good agreement between the QN model and the NQN model (see below). Another reason for this excellent agreement is the locality of the processes, which additionally reduces the influence of the above mentioned approximations.

For the neutral excited species, the flux is only determined by diffusion, i.e., $\vec{G}_s = -D_s\vec{\nabla}n_s$. The transport coefficients used in the above expressions are taken from reference.[23] The argon atom density is considered to be constant. Equation 1 is solved for the two types of ions and three types of excited species (Ar(4s), Ar(4p), and Ar_2^*).

Electron energy conservation equation: The electron energy conservation equation is solved for the averaged electron energy density $n_e\bar{\varepsilon}_e$:

$$\frac{\partial n_e\bar{\varepsilon}_e}{\partial t} + \vec{\nabla}\cdot\vec{G}_{\varepsilon,e} + (\vec{u}_g\cdot\vec{\nabla})n_e\bar{\varepsilon}_e = \sigma\vec{E}_{\mathrm{d}}^2 + n_e\Delta\bar{\varepsilon}_e + Q_{bg} \tag{7}$$

The expression for the electron energy flux $\vec{G}_{\varepsilon,e}$ in a reference frame moving with the gas is

$$\vec{G}_{\varepsilon,e} = -D_{\varepsilon,e}\vec{\nabla}(n_e\bar{\varepsilon}_e) - \mu_{\varepsilon,e}n_e\bar{\varepsilon}_e\vec{E}_{amb} \tag{8}$$

where $D_{\varepsilon,e}$ is the electron energy diffusion coefficient and $\mu_{\varepsilon,e}$ is the electron energy mobility, and the ambipolar electric field $\vec{E}_{amb}$ is derived from Equation 6 above.

The terms at the right hand side represent (i) the Joule heating term ($\sigma\vec{E}_d^2$), where σ is the plasma electric conductivity (see below), (ii) the averaged electron elastic and inelastic collision energy losses ($\Delta\bar{\varepsilon}_e$), and (iii) a constant background power density (Q_{bg}) as explained in.[23] Note that the approach of using a background power was also used by others in order to avoid model complications in the context of streamer propagation.[28,46] Indeed, if the background power density is properly chosen to be low enough, it does not affect the final results, but it improves the numerical convergence of the model. For the conditions of our simulations this was verified by multiple simulations with various values of Q_{bg}.

The particle conservation Equation 1 and the electron energy Equation 7 are solved in Comsol (version 4.3a) for the dependent variables $\ln(n_s)$ and $\ln(n_e\bar{\varepsilon}_e)$ instead of n_s and $n_e\bar{\varepsilon}_e$, respectively, in order to avoid the appearance of negative densities in the solution and to improve the numerical stability of the model.

Electric potential equation: It is common to eliminate the Poisson equation from the model under the assumption of QN, since the charge density is not available. Here, the current continuity equation is solved for the applied electric field E_{d}. Summing Equation 1 for the charged species, we derive

$$\vec{\nabla}\cdot(-\sigma\vec{\nabla}\phi) + |q_e|(D_{\mathrm{Ar}_2^+}\vec{\nabla}n_{\mathrm{Ar}_2^+} + D_{\mathrm{Ar}^+}\vec{\nabla}n_{\mathrm{Ar}^+} - D_e\vec{\nabla}n_e) = 0,$$

where ϕ is the electric potential and

$$\sigma = |q_e|\sum_s \mu_s n_s \tag{9}$$

is the plasma conductivity, obtained from the sum over the charged species only, i.e., for the considered chemistry, $\sigma = |q_e|(\mu_{\mathrm{Ar}_2^+}n_{\mathrm{Ar}_2^+} + \mu_{\mathrm{Ar}^+}n_{\mathrm{Ar}^+} + \mu_e n_e)$. Neglecting the diffusion terms and considering only the external source of the electric field (driving potential ϕ_d) we obtain for the current continuity equation:

$$\vec{\nabla}\cdot(-\sigma\vec{\nabla}\phi_d) = 0 \tag{10}$$

Gas thermal balance equation: The gas thermal balance equation is

$$\rho C_p\frac{\partial T_g}{\partial t} + \rho C_p\vec{u}_g\cdot\vec{\nabla}T_g - \vec{\nabla}\cdot(k_g\vec{\nabla}T_g) = Q_g \tag{11}$$

where ρ is the gas density, C_p is the heat capacity at constant pressure, k_g is the gas thermal conductivity, and Q_g is a heat source accounting for energy transfer from the electrons to the heavy particles due to elastic and inelastic collisions.

The expression for the gas heat source is as follows

$$Q_g = \frac{3m_e m_{Ar}}{(m_e + m_{Ar})^2} n_e n_{Ar} k_{el} e(T_e - T_g) + \sum_i \Delta\varepsilon_i k_i n_e n_i \quad (12)$$

where k_{el} is the elastic collision rate coefficient, and $\Delta\varepsilon_i$, k_i, and n_i are the inelastic collision energy loss, rate coefficient and collision target density, respectively, for the ith inelastic collision. The electron and gas temperature are expressed in eV in Equation 12. As pointed out in reference,[23] only in the cathode layer the ion heating becomes considerable. So we do not need to consider the ion heating term, because we do not take the sheath into account in the QN model.

Gas flow equations: The neutral gas flow, which is responsible for the arc displacement, is derived by a simplified version of the Navier-Stokes equations, which provide a solution for the mass density and the mass-averaged velocity. The incompressible Navier-Stokes equations are solved for a Newtonian fluid, excluding the inertial term

$$\rho \frac{\partial \vec{u}_g}{\partial t} = \nabla \cdot (-p\vec{I} + \mu(\vec{\nabla}\vec{u}_g + (\vec{\nabla}\vec{u}_g)^T)) \quad (13)$$

$$\rho \vec{\nabla} \cdot \vec{u}_g = 0 \quad (14)$$

where p is the gas pressure, μ is the gas viscosity, $\vec{I}$ is the unit matrix and the superscript "T" stands for the tensor transpose operation. In our case, the Navier-Stokes equations are first solved separately, and subsequently, the obtained velocity distribution is used as input data in the other equations, describing the plasma behavior and the gas heating. To benchmark the QN model versus the NQN model, we take the above simplified gas description, because we are not focusing here on a specific experimental condition. Thus the gas flow model is needed here only to provide a gas velocity distribution with well pronounced variation in the domain (from zero at the walls to maximum velocity in the center), but the exact velocity profile is not critical. However, in section 3 below, where a particular discharge is studied, we will use a much more accurate gas flow description, based on a turbulent model.

2.1.4. QN Axisymmetric Model

The QN axisymmetric model includes the following equations from above: Equation 1 for the ions and the excited species, as well as Equation 7, 10, and 11, using again the expressions 2, 3, 6, 8, and 12. There are two differences compared to the QN Cartesian model, namely, (i) the gas flow is not described (i.e., we do not solve Equation 13 and 14) and (ii) the convection terms in Equation 1, 7, and 11, i.e., $(\vec{u}_g \cdot \vec{\nabla})n_s$, $(\vec{u}_g \cdot \vec{\nabla})n_e\bar{\varepsilon}_e$, and $\rho C_p \vec{u}_g \cdot \vec{\nabla} T_g$, are replaced with an effective convection term, $n_s \nu_{conv}$, $n_e\bar{\varepsilon}_e\nu_{conv}$, and $\rho C_p(T_g - 293)\nu_{conv}$, respectively, representing effectively the influence of elongation and/or relative velocity between the arc and the background gas flow with a parameter ν_{conv}, called the convection frequency (see details in[24,31]). In general we write the variation of a conserved variable α (i.e., species density, electron energy density, etc.) as a function of ν_{conv}, i.e., $\partial\alpha/\partial t = (\alpha - \alpha_{bg})\nu_{conv}$, where α_{bg} is a background or minimum possible value. The contribution of the arc elongation to the effective convection frequency can be expressed as the ratio of the elongation velocity and the arc length $\nu_{conv} = v_{elong}/L_{arc}$. The contribution of the different velocity of the arc and the gas flow (i.e., arc slip with respect to the gas) can be approximated with $\nu_{conv} = v_{rel}/(\pi R_{arc}/2)$, where v_{rel} is the relative velocity between the arc and the gas flow and R_{arc} is the arc radius. The frequency considered in these simulations is $\nu_{conv} = 5$ kHz, which is the same as in[24] and it corresponds approximately to the experimental conditions in[29].

2.1.5. Boundary Conditions

The above partial differential equations are subjected to appropriate boundary conditions. The boundary conditions for the NQN models are described in detail in.[23] For the QN models we set zero species fluxes and zero electron energy flux at all boundaries. A thermal insulation condition is used for the gas heat balance equation. For the electric potential equation, the cathode potential V_c is derived from Ohm's law based on the value of the total arc current at the cathode, the external resistor value and the total applied voltage (i.e., voltage drop over the resistor and the arc). The anode is connected to the ground. For the Cartesian model, we must also provide boundary conditions for the gas flow. We use the same boundary conditions as for the gas flow in the NQN model, given in detail in.[23] At the gas inlet, the velocity is adjusted to be similar to the inlet velocity observed in experiments.[29] At the gas outlet, the gas pressure is set to 101 kPa. On the cathode and anode walls, the velocity follows a so-called "no slip" boundary condition, i.e., zero tangential velocity.

Finally, the external circuit and the power supply need to be specified. Like in reference,[24] the voltage source is fixed to 3700 V, and different resistances are used to limit the current to about 30 mA.

2.2. Results and Discussions

In order to validate the accuracy of the QN model applied to a GAD, we compare the results of the QN model with those of a NQN model, within both the 2D axisymmetric and Cartesian geometry. The similarities and differences between the two

models are discussed. We start the comparison with the axisymmetric models, since they are easily comparable and since we can easily show the difference in the near electrode regions and the arc body.

2.2.1. Comparison of QN and NQN Models Within a 2D Axisymmetric Geometry

Figure 2 presents the electron density spatial distribution for both models in the axisymmetric geometry. It can be seen that the arc is very similar, except in the near-electrode regions. The difference near the walls is expected, since there is no sheath in the QN model. In the NQN model, a small cathode spot is formed in order to provide the strong electric field needed for efficient field emission.

Most of the results in this subsection are presented at time 0.2 ms. This time is chosen in order to have sufficient time for the development of the typical bended arc (Figure 6). The particular moment of 0.2 ms is not special and similar results could be presented for other moments of times. The evolution of the arc in both the QN and NQN model is the same for the axisymmetric case but slightly shifted in the Cartesian models, as it will be shown in Figures 6–8.

The similarities and differences in the results can be better visualized in 1D plots of the various physical quantities. The electron number density distribution along the symmetry axis at $t = 0.2$ ms is given in Figure 3. Apart from the near-electrode regions, the electron number density is almost identical for both models.

A minor difference is observed in the potential distribution along the symmetry axis, plotted also in Figure 3, mainly as a result of the sheaths near the electrodes, which are not considered in the QN model. The electric field (i.e., the slope of the potential profiles) is calculated to be 17.04 kV/m and 16.86 kV/m for the NQN and QN models, respectively.

Figure 4 presents the radial distribution of the electron density and gas temperature at $z = 3$ mm (i.e., in the middle between cathode and anode) and $t = 0.2$ ms. The electron density and gas temperature exactly coincide for both models.

Finally, the comparison of the radial profiles of the ion densities is shown in Figure 5. Similarly to the electron density and gas temperature, the ion density profiles of the QN model are the same as those in the NQN model. The number density of atomic ions decreases monotonically while the density of the molecular ions increases first and then decreases in the radial direction. This behavior of the ion densities is related to the magnitude of the gas temperature, which influences the chemical reaction rate of atomic ion to molecular ion conversion, as discussed in reference,[47] where a similar behavior was observed.

In general, the plasma characteristics obtained with the QN model almost coincide with those of the NQN model; the results are the same, except for the electric potential distribution, which is somewhat shifted due to the sheaths. We expect that the small difference is a result of the approximations made in the QN model. Indeed, we assumed that the fluxes of positive and negative species are equal. In reality this is not entirely true since we apply a

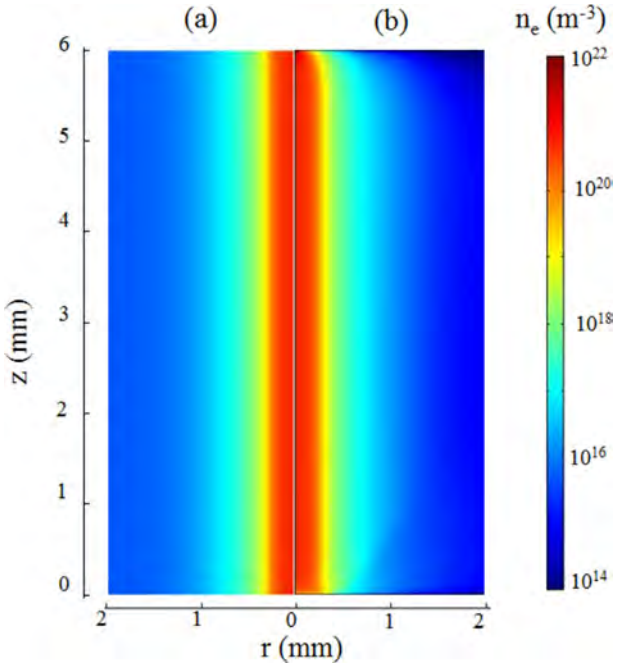

Figure 2. Electron density distribution, obtained by the QN (a) and NQN model (b) within the axisymmetric geometry at $t = 0.2$ ms and $I = 31$ mA. The anode is positioned at $z = 0$ mm, whereas the cathode is positioned at $z = 6$ mm.

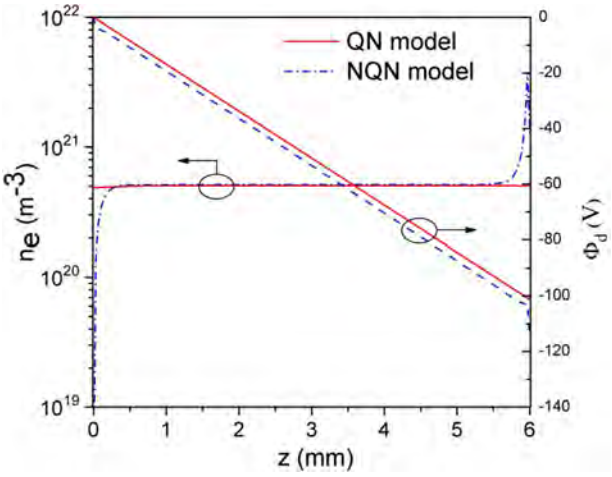

Figure 3. Electron density and electric potential (ϕ_d) distribution along the symmetry axis ($r = 0$) at $t = 0.2$ ms. The anode is positioned at $z = 0$ mm, whereas the cathode is positioned at $z = 6$ mm.

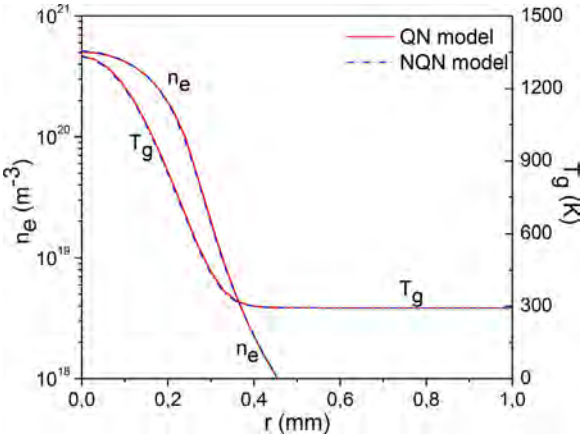

Figure 4. Radial distribution of electron density and gas temperature at $z = 3$ mm (i.e., in the middle between cathode and anode) and $t = 0.2$ ms.

voltage on the electrodes and the applied potential drives the electrons and the ions in opposite directions. In principle, we could overcome this limitation of the QN model by introducing an additional balance equation for the electrons, and proper boundary conditions at the boundary sheath – quasineutral plasma, as mentioned in section 2.1.3 above. However, this adds considerable complexity in the model and requires additional computation resources. The results presented above show that the difference is very small and the introduced error is minor, certainly in view of the reduction in calculation time. Probably the unknown uncertainty in the collision data (i.e., cross sections and rate coefficients) might introduce greater uncertainties in the final results than the effect of the assumptions made in the derivation of the QN model. The

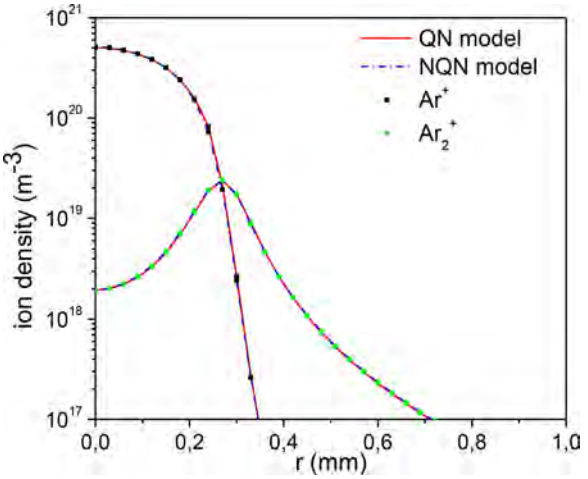

Figure 5. Radial distribution of the ion number densities at $z = 3$ mm (i.e., in the middle between cathode and anode) and $t = 0.2$ ms.

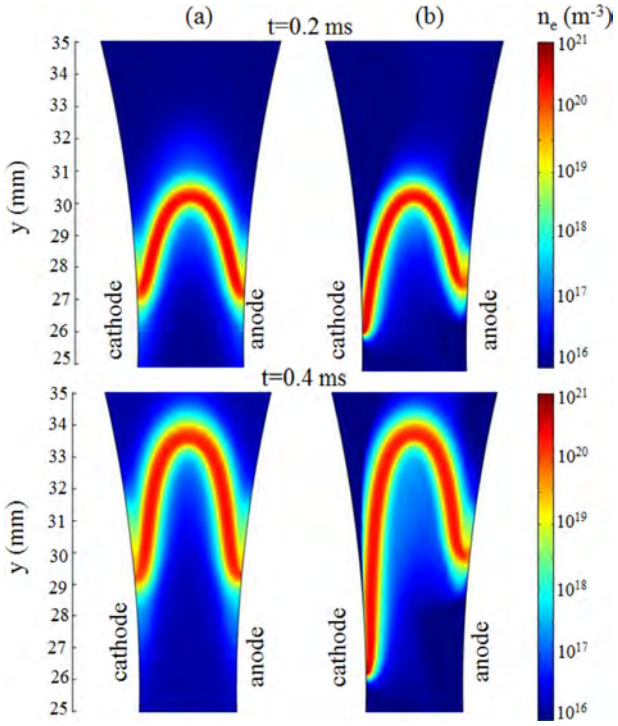

Figure 6. Electron density distribution, obtained by the QN (a) and NQN model (b) within the Cartesian geometry, at two different times.

main reason for the small effect of the equal fluxes approximation is the small contribution of the diffusion terms in the balance equations, which is a result of the atmospheric pressure operation of the discharge.

2.2.2. Comparison of QN and NQN Models Within a 2D Cartesian Geometry

The validation of the QN model is further extended to a Cartesian geometry with gas flow and gas/plasma convection. We compare the results from the two models within the Cartesian geometry, which reveals the arc gliding along the electrodes and thus describes a specific property of GADs. Figure 6 presents the electron density distribution of the Cartesian models at two different times. The arc calculated with the QN model continuously moves downstream along the electrodes as time progresses, due to the absence of a sheath region in this model, while in the NQN model, the arc attaches to a specific position of the cathode, which leads to the elongation of the plasma column with time. The process of the arc gliding was explained in detail in.[23,24] Here an important question arises: does the different arc column length result in different arc plasma characteristics? In order to answer this question, we compare the plasma characteristics along the *y* axis (at the center between cathode and anode) between the two models.

Figures 7 and 8 present the electron density and gas temperature profiles along the y axis at two different moments in time. The QN model shows its maxima 0.1 mm earlier in space than the NQN model, but this difference is certainly acceptable. From these figures we can see that the electron density and gas temperature obtained with the QN model agree well with the NQN model in the arc column region at different times. Although the arc length is different, the plasma characteristics are practically the same outside the cathode and anode regions. This confirms once again the reliability of the QN model as a tool to study the arc column characteristics, apart from the electrode regions. This is very important for future theoretical studies of the GAD, because the QN model allows modelling in a more realistic three-dimensional geometry within a reasonable computation time.

In summary, the comparison between QN and NQN models in both geometries shows clearly an excellent agreement outside the near electrode regions. The QN model does not describe the sheath regions and considers only the quasineutral plasma region. The speed up, provided by using the QN model versus the NQN model, is roughly 500%, but this number is highly dependent on model/configuration/conditions/solver and should not be taken as an exact measure. In any case, the model convergence rate of the QN model is much faster.

In the following two subsections we apply and demonstrate the viability of the QN approach for two different complex discharge conditions which are extremely difficult to model with a NQN model. The QN model is not validated directly for the conditions of these discharges because the use of NQN model for them is impractical. However, we expect that the QN model is still valid for these conditions since there is no reason to expect that the assumptions in the model fail for the considered discharges. Despite the discharge complexity, the quasi-neutrality conditions should be still valid outside the electrode regions and the equality of fluxes (Equation 4) should lead to similar effects since the major transport coefficients are of similar order.

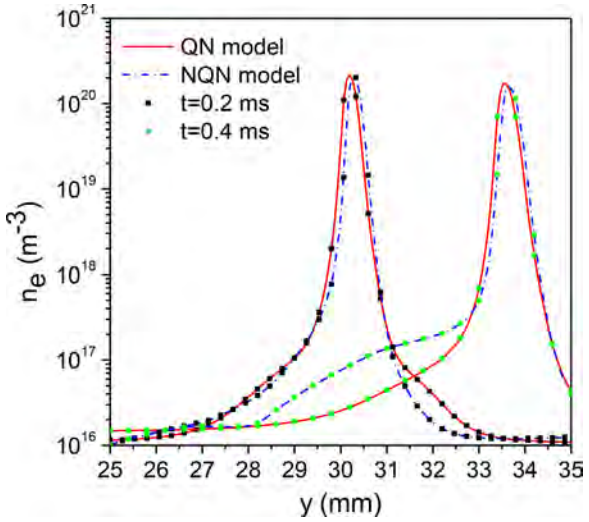

Figure 7. Electron density distributions along the y axis at the center between cathode and anode, obtained by the QN and NQN model within the Cartesian geometry, at two different times.

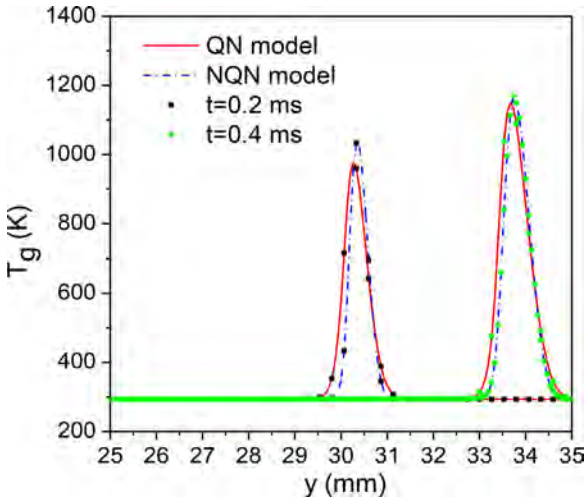

Figure 8. Gas temperature distributions along the y axis at the center between cathode and anode, obtained by the QN and NQN model within the Cartesian geometry at two different times.

3. 3D QN Model of a Reverse-Vortex Plasmatron

As a result of the reduced computational cost of the QN model, we are now able to describe complex three-dimensional geometries, albeit still with simplified chemistry. In this section we demonstrate the use of the QN model for the numerical simulation of a GAD with a RVF configuration, also called "plasmatron." This discharge is envisaged as an efficient method for flow confinement in a gliding arc discharge and shows very promising results for CO_2 decomposition.[3,4] The device consists of a tube or a cylindrical vessel with tangentially oriented inlets (Figure 9), which provoke a strong tangential flow along the walls. As the flow reaches the bottom of the reactor (the side where it cannot leave), it continues its movement in the inner vortex in the opposite direction and exits the tube through the outlet, which is located on the same side as the inlets. This essentially forces an inner vortex in the opposite direction with respect to the outer vortex, hence: reverse-vortex flow. The model presented in this section is meant to make a step forward in low-temperature plasma modelling by incorporating effects such as flow turbulence in a three-dimensional geometry.

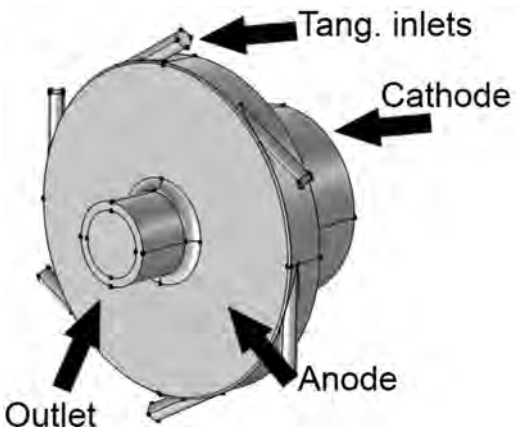

Figure 9. Inner structure of the RVF GAD reactor, or plasmatron, used as model geometry.

3.1. Model Description

3.1.1. Model Geometry

The considered device consists of a tube-like reactor with 6 tangential inlets and interchangeable electrodes. The cathode is located on the back as an interchangeable cap. The anode is on the front, acting as an outlet as well. The reactor is 23 mm long, and is configured with a 3.81 mm outlet radius. The cathode radius is 8.85 mm. The length of the wider region with the tangential inlets is 30.5 mm and its length is 4 mm.

3.1.2. Gas Flow Modeling

The considered flow rate is 22.8 L/min, which corresponds to strong velocity gradients and high turbulence. At such conditions, solving the Navier-Stokes equations for flow modeling would require a very fine discretization mesh (direct numerical simulation) and too much computing power. For this reason, a turbulence model is employed, namely the k-ε RANS (Reynolds-Averaged-Navier-Stokes) model. With this method, the oscillating turbulent quantities and eddies are averaged over time, for a smooth, stationary solution. The k-ε RANS system of equations is further coupled to the gas thermal balance equation using Kays-Crawford model to account for the turbulent heat dissipation. As is shown in section 3.2 below, the turbulent heat transfer plays a significant role for calculating the final gas temperature. The whole system of equations, governing the gas flow and the gas heat balance is presented in detail in Appendix A.

3.1.3. Plasma Modeling

The plasma model uses the QN description as given in subsection 2.1.3, but with a reduced electron impact reaction set for argon, compared to section 2. Only one type of ions (Ar^+) and one type of excited species (Ar[4s]) are considered. The reactions taken into account in the model can be found in.[25] The purpose of having a very limited reaction set is to reduce the computation time, which is essential for three-dimensional models. A detailed description of the model boundary conditions can also be found in.[25] The gas and plasma models are solved with COMSOL Multiphysics version 5.0. The discretization mesh consists of about 150 000 elements.

3.2. Results and Discussion

In Figures 10 and 11, the gas velocity streamlines and distribution are presented. The results are a steady state solution for the gas flow only, without plasma. The formation of the reverse-vortex flow can be clearly observed in Figure 10, with the flow rotating near the wall toward the closed end of the reactor and then an inner vortex is formed moving the gas toward the outlet with relatively low velocity (the blue lines). The cross-section at Figure 11 shows the velocity maximum at the midpoint between the reactor inlets and center.

With the obtained stationary solution for the gas flow variables and turbulent dissipation rates, the plasma model is computed as a time-dependent solution, without solving again the gas flow equations but only gas thermal balance. The model continuously computes the outputs from the equations, which are coupled in a unified solution. It takes about 300 h to compute 1 ms of model time on a workstation equipped with a Xeon E5-2697 CPU with 256GB of RAM.

In Figures 12 and 13, the plasma density and gas temperature are illustrated, as calculated by the plasma

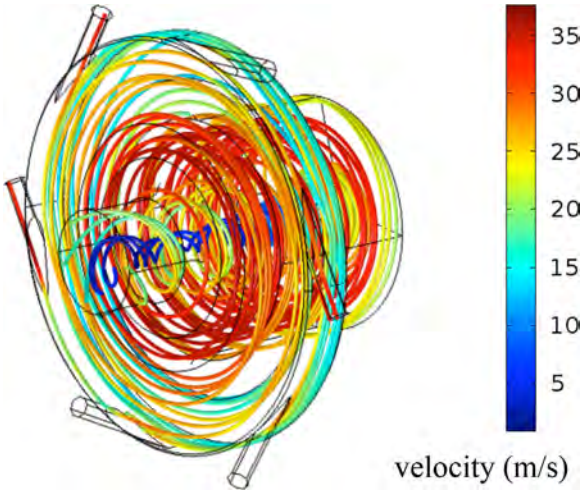

Figure 10. Streamlines of the reverse-vortex inside the plasmatron (see geometry in Figure 9). The flow velocity is expressed in the color legend.

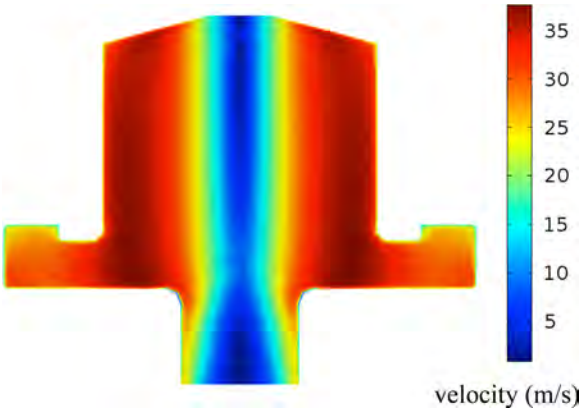

Figure 11. Velocity plot over a central cross-section of the plasmatron.

model, 1 ms after the channel initiation. The arc is initiated at a radial position of 5.65 mm. With time, the arc rotates by following the vortex gas flow (cf. Figure 10) and gradually moves toward the discharge axis. After 1 ms the arc has not yet reached a quasi-stationary state, i.e., rotation at the same trajectory. Usually the arc is stabilized in such a state when it rotates near the discharge axis and the arc plasma-electrode contact is at the output nozzle, as in.[25] The values for the plasma density are comparable to [25], while the gas temperature is significantly lower than in[25] due to the addition of turbulent heat transfer (see Figure 14 below). Indeed, the analysis of the results shows that the turbulent thermal conductivity $k_{g,Tu}$ (see Appendix A) is around two orders of magnitude higher than the gas conductivity k_g, and thus it contributes noticeably to the overall heat transfer. Without turbulent heat transfer, the major channel for heat exchange in the arc is related to the

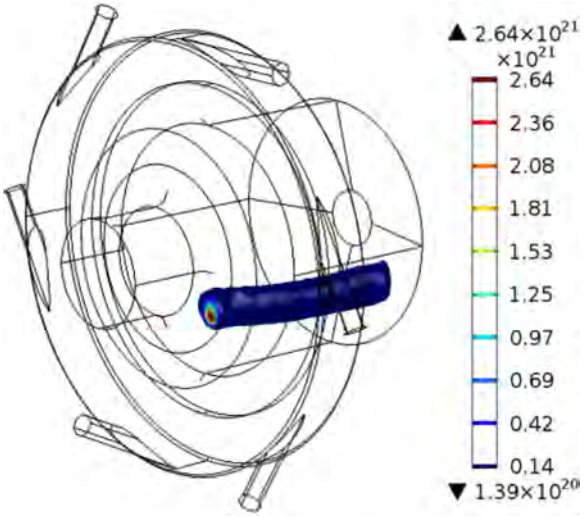

Figure 12. Plasma density [m^{-3}], isosurface plot (10 levels), at 1 ms, 1.3 A of arc current.

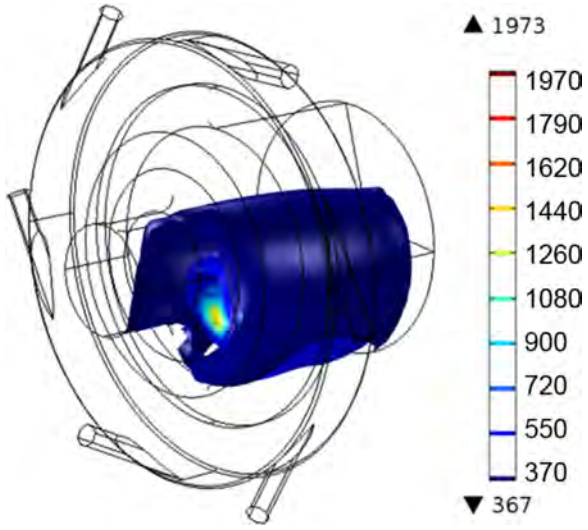

Figure 13. Gas temperature [K], isosurface plot (10 levels), at 1 ms, 1.3 A of arc current.

convection processes and the conduction term is small. Accounting for the turbulent transport through effective parameters (like $k_{g,Tu}$), makes the conduction term in Equation 11 (see section 2.1.3 above) significant for the considered configuration and conditions, and within the arc even larger than the convective term, thus allowing more efficient cooling of the gas in the arc central parts toward the colder gas outside the arc.

The electron temperature (Figure 15) is rather high for this type of discharge, but this is probably related to the very simplified chemistry, which underestimates the total ionization rate and thus a higher electron temperature is needed to sustain the discharge with certain electron density, allowing the flow of the electric current, determined by the external circuit.

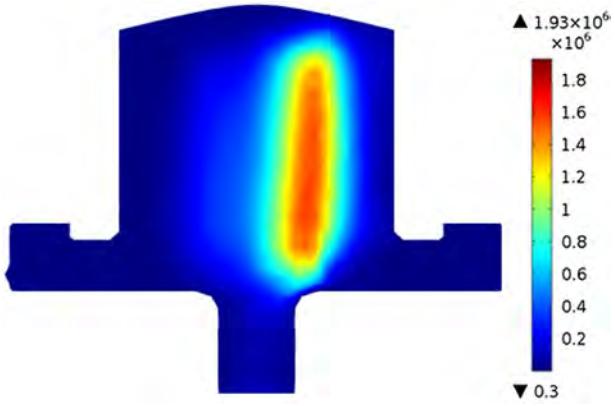

Figure 14. Turbulent heat flux [W/m^2], cross-section of the reactor at 1 ms, 1.3 A of arc current.

4. 1D QN Model of a Gliding Arc Discharge in CO_2

Finally, in this section, we apply the QN model to a GAD operating in CO_2. Indeed, the conversion of CO_2 in plasma is a hot topic nowadays and a lot of research effort is performed on this topic. The use of GADs for this application is an attractive path due to the very simple discharge design and the need of small initial investment. However, the energy efficiency is a key factor for the successful adoption of these devices. The complexity of the plasma chemistry is a significant barrier for a complete and thorough numerical study of these discharges. Models of CO_2 plasma usually account for hundreds of species and therefore they are usually limited to 0D.[22,34,35,48–50] The large number of species and related chemical reactions occurring in a non-equilibrium CO_2 plasma makes spatially resolved models computationally expensive. In order to solve this problem, we have developed a 1D quasi-neutral, quasi-gliding arc model in a cylindrical frame, with a reduced – but still detailed – non-equilibrium CO_2 plasma chemistry, including the CO_2 vibrational kinetics, in order to obtain a better understanding of the basic CO_2 plasma chemistry in a GAD.

The model used in this section is presented in details in.[31] Here only a brief overview is given. The results presented here give a different perspective of the discharge time evolution, not presented in,[31] but they are derived for conditions similar to[31] and therefore both give similar trends. The difference is the convection frequency which is twice a high compared to.[31]

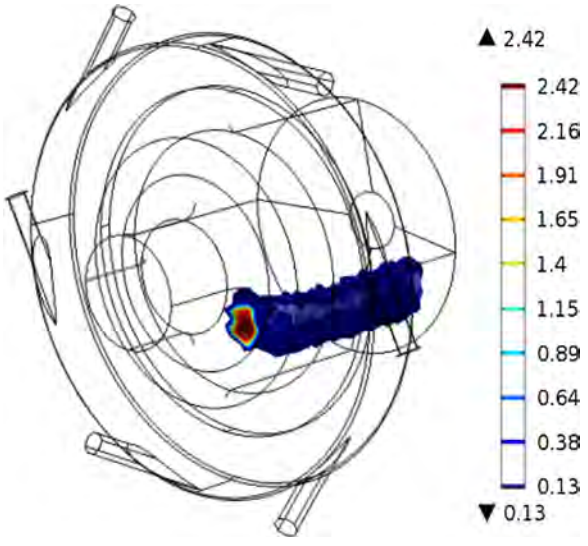

Figure 15. Electron temperature [eV], isosurface plot (10 levels), at 1 ms, 1.3 A of arc current.

4.1. Model Description

4.1.1. Geometry and Treatment of Convective Cooling in the Model

In this model, we take into account a transverse cross section of the plasma string along the symmetry plane of the reactor, excluding the longitudinal coordinate along the discharge current. The gliding arc is then simply described as a conducting channel in an axi-symmetrical cylindrical geometry. The loss of plasma species and energy due to convection in the arc are considered by introducing an effective convective frequency (as explained in subsection 2.1.4) of the gas in the arc, which allows our model to better represent the specific properties of the gliding arc.[24,31].

4.1.2. CO_2 Plasma Chemistry Considered in the Model

The chemistry set is based on the full chemistry set developed by Kozák and Bogaerts [34,35], but somewhat reduced to include only the most important species and processes, while still accounting for the full vibrational kinetics. In total it includes five neutral ground state species (i.e., CO_2, CO, C, O_2, and O), five different ions (i.e., C_2^+, O_2^+, CO_3^-, O^-, and O_2^-), 25 CO_2 vibrational levels (i.e., 4 effective levels and the 21 levels of the asymmetric stretch mode, up to the dissociation limit), one electronically excited level of CO_2, and three vibrational levels of O_2, as well as the electrons. More details on the list of species considered in the model, as well as the entire reaction chemistry, can be found in.[31]

4.1.3. Equations Solved in the Model

The model calculates the plasma species densities, the electron and gas temperature and the electric field in the gliding arc. Similarly to the axisymmetric model discussed in subsection 2.1.4, the model used here is based on the QN approach and it includes again Equation 1, 7, and 11, in which the convection terms i.e., $(\vec{u}_g \cdot \vec{\nabla})n_s$, $(\vec{u}_g \cdot \vec{\nabla})n_e\bar{\varepsilon}_e$, and $\rho C_p \vec{u}_g \cdot \vec{\nabla} T_g$ are replaced with the effective convection terms, $(n_s - n_{s,\mathrm{bg}})\nu_{\mathrm{conv}}$, $n_e\bar{\varepsilon}_e\nu_{\mathrm{conv}}$, and $\rho C_p(T_g - 293)\nu_{\mathrm{conv}}$, respectively, where $n_{s,\mathrm{bg}}$ is the background (minimum) density for the species "s." The particle balance equations are solved for the electrons, all types of ions and excited species, except for CO_2^+ and the ground state of CO_2. Indeed, the number density of CO_2^+ is simply determined by electrical neutrality in the plasma, while the number density of ground state CO_2 is obtained by subtracting the sum of the number densities of all other species from the total species number density. The species flux is again given by Equation 2, but without the first term on the right hand side for the neutral species since $q_s = 0$. The ambipolar electric field $\vec{E}_{\mathrm{amb}}$ is derived from the various charged species:

$$\vec{E}_{amb} = \frac{D_{CO_2^+}\nabla n_{CO_2^+} + D_{O_2^+}\nabla n_{O_2^+} - D_{CO_3^-}\nabla n_{CO_3^-} - D_{O^-}\nabla n_{O^-} - D_{O_2^-}\nabla n_{O_2^-} - D_e\nabla n_e}{n_{CO_2^+}\mu_{CO_2^+} + n_{O_2^+}\mu_{O_2^+} + n_{CO_3^-}\mu_{CO_3^-} + n_{O^-}\mu_{O^-} + n_{O_2^-}\mu_{O_2^-} + n_e\mu_e} \quad (15)$$

The mobility and diffusion coefficients of the electrons and the various ions can be found in.[31]

The electric field is obtained from the total arc current I_{arc} as:

$$E_d = I_{arc} / \int_0^{r_{max}} 2\pi r\sigma dr \quad (16)$$

where the integral provides the electrical conductance of an arc channel with unit length, σ is again the plasma conductivity as given by Equation 9 and r_{max} is the size of the considered domain.

The set of 1D radially-dependent equations for the various species densities, the electron and gas temperature and the ambipolar electric field in the CO_2 plasma is again solved by means of COMSOL Multiphysics (version 5.0) in a cylindrical frame with maximum radius $r_{max} = 2$ mm. At the boundary of $r_{max} = 2$ mm, the same values as the background values for the solution variables are assumed (see above). More details about the model can be found in.[31]

4.2. Results and Discussion

In Figure 16, we present the time evolution of the discharge current and electric field (a), the electron temperature, vibrational temperature of the asymmetric mode of CO_2 and the gas (translational) temperature (b), as well as the molar fractions of the dominant neutral species and the electrons (c) at the center of the arc, for one half cycle of the applied (sinusoidal) current.

The electric field has a sharp peak at the very beginning (around 0.1 ms), related with the initial establishment of the arc. In the model we impose a sinusoidal current, but at the same time the initial electron density and thus the plasma conductivity are low. Following Ohm's law, an increasing current combined with a high resistance leads to a high voltage. Thus the electric field (determined by the arc voltage) increases sharply in order to produce more electrons by more intense ionization, and thus to allow the flow of the imposed current. Later the electric field drops to an almost constant value around 10^5 V/m and at the end of the current half cycle, it increases again slightly due to the drop in the electron density (Figure 16(c)).

The electron temperature (Figure 16(b)) shows an almost constant value around 31 000 K (or 2.7 eV), except at the beginning and at the end of the half cycle, which means that the electron energy loss and production processes are comparable. The gas temperature remains also almost constant around 2500 K, which is mainly due to the

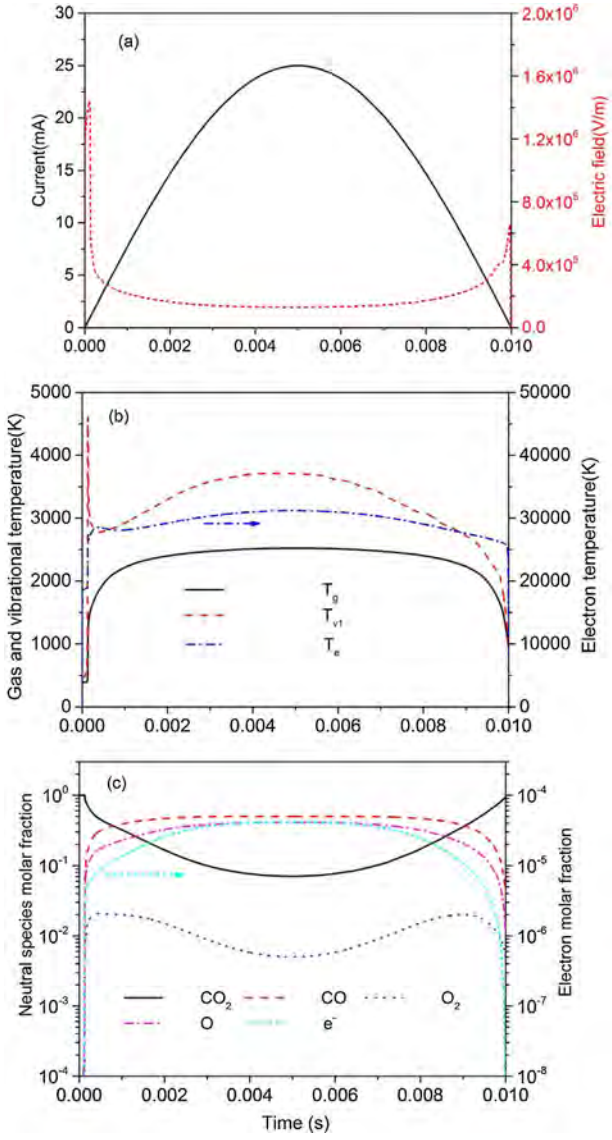

Figure 16. Time evolution of the discharge current ($I_{arc} = 25\sin(2\pi 50t)$ mA) and the electric field (dashed line) (a), the electron temperature T_e (right axis), the vibrational temperature of the asymmetric mode T_v (CO_2) and the gas (translational) temperature T_g (left axis) (b), and the molar fractions of the dominant neutral species and the electrons (c). Except I_{arc} and E_d (constant along r), all other quantities are shown at the center of the arc ($r = 0$ mm) The characteristic frequency of convective cooling is 5 kHz.

imposed effective convective losses. At the considered conditions, the gas thermal conductivity is rather insignificant and the arc cooling is accomplished mainly by the effective convective heat losses (see section 2.1.4). Finally, the vibrational temperature of the asymmetric stretch mode of CO_2 is around 3700 K, hence somewhat higher than the gas temperature, indicating the overpopulation of the vibrational states of CO_2, which can promote the effective dissociation.

Figure 16(c) illustrates the time-evolution of the molar fractions of the dominant species at the arc center. There is a well pronounced depletion of CO_2 corresponding to the current maximum. This is a result of the CO_2 conversion into CO and O, which indeed have quite high molar fractions. At the end of the current half cycle, the CO_2 density increases and restores its initial value. The latter is because of recombination between CO and O. These results do not yet allow to obtain information of the overall CO_2 conversion in the GAD, since one needs to account for the effective fraction of the gas passing through the arc. For this purpose, a 2D model will be needed, which is currently under development.

5. Conclusion

In this work the plasma and gas characteristics of various types of GAD configurations are calculated and analysed with a QN plasma model, coupled to an appropriate gas flow description. Due to the approximations made in the development, the QN model is first compared with the results obtained from a more elaborate NQN model, in 2D within both axisymmetric and Cartesian geometries. The different geometries show the different aspects of the discharge. Although a comparison with experiment would even be better in order to test the reliability of the QN model, it is difficult at this stage, because of the limited dimensionality of the 2D model, but it will be pursued in our future work.

The QN model presented here neglects the near-electrode regions and treats only the quasineutral plasma region. Although there are small differences in the plasma characteristics obtained with the QN and NQN model, which are attributed to the approximations made in the derivation of the QN model, in general, the results of the QN model agree very well with those of the NQN model in the arc column region. This indicates that the QN model provides a reliable description of the arc column characteristics, neglecting the contact regions between the arc and the electrodes. This result is of major importance for model developments of the GAD in three-dimensions or with more detailed plasma chemistries, because it shows that the QN model approach can be safely used for these purposes, as long as we do not focus on the near-electrode regions, at only about 20% of the computation cost of a NQN model.

It is important, however, to also clearly point out the disadvantages of the QN model. The lack of wall sheaths in the model does not allow the modelling of any effect related with electrode-arc interaction. For example the attachment of the arc[30] to electron emission centres[23] cannot be observed and all consequences of this effect in principle are lost. The arc attachment might lead to a significantly longer arc[30] compared to what we obtain without any attachment. This might be a problem when one tries to estimate the active volume of the arc and eventually the volume of treated gas, in conditions favouring the arc attachment. This drawback of the QN model can be partially overcome by an artificially forced arc attachment to certain points and detachment from them, governed by certain parameter(s) or a probability distribution. This will be considered as a possibility in the future.

Another disadvantage of the QN model is the lack of information for the power losses at the walls/electrodes. In,[24] it was shown that in a glow regime, the power loss at the cathode can be significant. One could, however, use a NQN axially symmetric model to obtain typical values of the power losses at the electrodes and later use that information for the power balance of the discharge, described by the QN model.

The applicability of the QN model is illustrated for two model systems, i.e., a three-dimensional model for a RVF GAD and a 1D model for a GAD in CO_2. The three-dimensional RVF GAD model cannot be described with a full NQN model, because of prohibitively long calculation times. The model shows that a complex discharge geometry with complex gas flow can now be described with a QN model in three-dimensional, coupled with elaborate gas flow description, but with very simplified chemistry. The simulation results show a significant effect of the turbulent heat transport on the gas heating and cooling, leading to a reduced gas temperature.

The modelling of complex plasmas like a CO_2 discharge also benefits from the faster QN model calculation. This 1D model includes a detailed plasma chemistry, accounting also for the CO_2 vibrational levels. Some characteristic results are illustrated, such as the molar fractions of the various plasma species, and the gas temperature, electron temperature and CO_2 vibrational temperature, demonstrating the non-equilibrium characteristics of the GAD, with a much higher electron temperature than the gas and vibrational temperature.

This work provides a solid foundation for the further development of gliding arc models in three-dimensional, as well as in 2D where the focus can be on specific aspects of the gliding arc behavior, or on complex plasma chemistries, which will be the subject of our future work.

Acknowledgments: This work is financially supported by the Methusalem financing of the University of Antwerp, the European Marie Skłodowska-Curie Individual Fellowship project "GlidArc" within Horizon2020, the Fund for Scientific Research Flanders (FWO; Grant no. G.0383.16N and 11U5316N) and the IAP/7 (Inter-university Attraction Pole) program "Physical Chemistry of Plasma-Surface Interactions" from the Belgian Federal Office for Science Policy (BELSPO). The work was carried out in part using the Turing HPC infrastructure of the CalcUA core facility of the Universiteit Antwerpen, a division of the Flemish Supercomputer Center VSC, funded by the Hercules Foundation, the Flemish Government (department EWI) and the Universiteit Antwerpen. This research was also supported by Sofia University, grant no 67/12.04.2016.

Appendix A

Some more details are given about the turbulent mass and heat transfer model used for the description of the gas flow and heat balance of the RVF GAD in section 3.

k-ε Model

The k-ε Reynolds-averaged Navier-Stokes (RANS) model is a well-known method for computing gas flows with high degrees of turbulence.[51–54] It is one of the most common models, and it uses a system of two transport equations to solve for the gas parameters – velocity field and pressure.

$$\nabla \cdot (\rho \vec{u}_g) = 0 \tag{A.1}$$

$$\rho(\vec{u}_g \cdot \nabla)\vec{u}_g = \nabla \cdot \left[-p\vec{I} + (\mu + \mu_{Tu})\left(\nabla \vec{u}_g + \nabla(\vec{u}_g)^T\right) - \frac{2}{3}(\mu + \mu_{Tu})(\nabla \cdot \vec{u}_g)\vec{I} - \frac{2}{3}\rho k_{Tu}\vec{I}\right] + \vec{F} \tag{A.2}$$

Equation A.1 and A.2 represent the mass and momentum continuity system in the k-ε RANS model, where ρ stands for the gas density, $\vec{u}_g$ is the gas flow velocity vector, superscript T stands for transposition, p is the gas pressure, μ is the dynamic viscosity of the fluid, μ_{Tu} is the turbulent viscosity of the fluid, k_{Tu} is the turbulent kinetic energy, $\vec{I}$ is the unity tensor, and $\vec{F}$ is the body force vector. The equations are coupled with another system solving for the turbulent kinetic energy and the turbulent dissipation ε_{Tu}:

$$\rho(\vec{u}_g \cdot \nabla) = \nabla \cdot \left[\left(\mu + \frac{\mu_{Tu}}{\sigma_k}\right)\nabla k_{Tu}\right] + P_k - \rho\varepsilon_{Tu} \tag{A.3}$$

$$\mu_{Tu} = \rho C_\mu \frac{k_{Tu}^2}{\varepsilon_{Tu}} \tag{A.4}$$

$$P_k = \mu_{Tu}\left[\nabla \vec{u}_g : \left(\nabla \vec{u}_g + (\nabla \vec{u}_g)^T\right) - \frac{2}{3}(\nabla \cdot \vec{u}_g)^2\right] - \frac{2}{3}\rho k_{Tu}\nabla \cdot \vec{u}_g \tag{A.5}$$

Equation A.3, A.4, and A.5 compute the kinetic energy transport, the turbulent viscosity and the production term for k_{Tu}. The model constants σ_k and C_μ are adopted from literature.[51] The k-ε model does not solve for the flow near the walls; instead it uses wall functions, i.e., the viscous layer at the boundary areas is approximated by analytical expressions. The turbulent flow near a wall can be divided into three main regions: a thin viscous layer attached to the wall, a buffer layer, which appears as a transitional zone between the viscous (or laminar) layer and the free turbulent stream, and the turbulent free stream itself. It is easy to see that the modelling for these regions can be quite challenging, as they introduce a large gradient for the flow velocity. For this reason, the velocity near the walls is approximated by the so-called "wall functions," especially for models suitable for high-Re flows such as the k-epsilon model.[51] Essentially, the laminar layer is ignored, and an additional source term is added in the momentum conservation equation, which gives an interpolation of the velocity gradient multiplied by viscosity:

$$\left[(\mu + \mu_T)\left(\nabla \vec{u}_g + \nabla(\vec{u}_g)^T\right) - \frac{2}{3}(\mu + \mu_T)(\nabla \cdot \vec{u}_g)\vec{I} - \frac{2}{3}\rho k_T \vec{I}\right]\vec{n} = -\rho\frac{u_\tau}{\delta_w}\vec{u}_{tang}$$

$$\varepsilon = \rho\frac{C_\mu k^2}{k_v \delta_w \mu}$$

where $\vec{n}$ is the normal vector, δ_w is the wall distance, u_τ is the flow velocity at the wall, $\vec{u}_{tang}$ is the tangential flow vector and k_v is the turbulent kinetic energy at the wall boundary.

As a result, the calculation time for the model is much shorter and the stability is greater. However, the flow velocity at the wall is non-zero, which should be taken into consideration for precise simulations.

Heat Equation and Turbulent Heat Transfer

The gas thermal balance relies on the heat source and the equation that governs it. In the model, the heat equation 11 is solved for the gas. The Kays-Crawford model accounts for the turbulent heat transfer.[55] It is derived using the turbulent Prandtl number, which is the ratio of the momentum eddy diffusivity and heat transfer eddy diffusivity. The model is defined as:

$$Pr_T = \left(\frac{1}{2Pr_{T\infty}} + \frac{0.3}{\sqrt{Pr_{T\infty}}}\frac{C_p\mu_{Tu}}{k_g} - \left(0.3\frac{C_p\mu_{Tu}}{k_g}\right)^2\left(1 - e^{-k_g/\left(0.3C_p\mu_{Tu}\sqrt{Pr_{T\infty}}\right)}\right)^{-1}\right) \tag{A.6}$$

where Pr_T is the turbulent Prandtl number and $Pr_{T\infty}$ is the turbulent Prandtl number at infinity (~0.85). Thus, the thermal conductivity as a result of the turbulent transport is found as $k_{g,Tu} = C_p\mu_{Tu}/Pr_T$. This expression is added to the thermal conductivity k_g in Equation 11 when a turbulent transport is considered.

Received: June 30, 2016; Revised: September 19, 2016; Accepted: September 20, 2016; DOI: 10.1002/ppap.201600110

Keywords: carbon dioxide conversion; computer modelling; gliding arc discharges; non-thermal plasma; reverse-vortex flow

[1] A. Fridman, S. Nester, L. A. Kennedy, A. Saveliev, O. Mutaf-Yardemci, *Prog. Energy Combust. Sci* **1999**, *25*, 211–231.
[2] A. Czernichowski, *Pure& Appl. Chem*. **1994**, *66*, 1301–1310.
[3] A. Fridman, *Plasma Chemistry*, Cambridge University Press, New York, US **2008**.
[4] T. Nunnally, K. Gutsol, A. Rabinovich, A. Fridman, A. Gutsol, A. Kemoun, *J. Phys. D: Appl. Phys* **2011**, *44*, 274009.
[5] S. Gangoli, A. Gutsol, A. Fridman, *Plasma Sources Sci. Technol*. **2010**, *19*, 065003.
[6] V. Dalaine, J. M. Cormier, P. Lefaucheux, *J. Appl. Phys*. **1998**, *83*, 2435.
[7] V. Dalaine, J. M. Cormier, S. Pellerin, P. Lefaucheux, *J. Appl. Phys*. **1998**, *84*, 1215.
[8] X. Tu, J. C. Whitehead, *Int. J. Hydrogen Energy* **2014**, *39*, 9658.
[9] JL Liu, HW Park, WJ Chung, DW Park, *Chem. Eng J* . **2016**, *285*, 234.
[10] J L Liu, H W Park, W J Chung, D W Park, *Plasma Process*. **2016**, *36*, 437.
[11] K Li, JL Liu, XS Li, X Zhu, AM Zhu, *Chem. Eng. J*. **2016**, *288*, 671.
[12] Y. Kusano, B. F. Sørensen, T. L. Andersen, H. L. Toftegaard, F. Leipold, M. Salewski, Z. Sun, J. Zhu, Z. Li, M. Alden, *J. Phys. D: Appl. Phys*. **2013**, *46*, 135203.
[13] A. Fridman, A. Gutsol, S. Gangoli, Y. Ju, T. Ombrello, *J. Propul. Power* **2008**, *24*, 1216–1228.
[14] J. Zhu, J. Gao, A. Ehn, M. Alden, Z. Li, D. Moseev, Y. Kusano, M. Salewski, A. Alpers, P. Gritzmann, M. Schwenk, *Appl. Phys. Lett*. **2015**, *106*, 044101.
[15] X. Tu, H. J. Gallon, J. C. Whitehead, *IEEE Trans. Plasma Sci*. **2011**, *39*, 2900–2901.
[16] G. Xu, X. Ding, *Plasma Sci*. **2012**, *40*, 3458–3464.
[17] F. Richard, J. M. Cormier, S. Pellerin, J. Chapelle, *J. Appl. Phys*. **1996**, *79*, 2245–2250.
[18] O. Mutaf-Yardimci, A. Saveliev, A. Fridman, L. Kennedy, *J. Appl. Phys*. **2000**, *87*, 16321641.
[19] I. Kuznetsova, N. Kalashnikov, A. Gutsol, A. Fridman, L. Kennedy, *J. Appl. Phys*. **2002**, *92*, 42314237.
[20] S. Pellerin, J-M. Cormier, F. Richard, K. Musiol, J. Chapelle, *J. Phys. D: Appl. Phys*. **1999**, *32*, 891897.
[21] S. Pellerin, F. Richard, J. Chapelle, J-M. Cormier, K. Musiol, *J. Phys. D: Appl. Phys*. **2000**, *33*, 24072419.
[22] A. Indarto, J-W. Choi, H. Lee, H. K. Song, *J. Natural Gas Chem*. **2005**, *14*, 13–21.
[23] St. Kolev, A. Bogaerts, *Plasma Sources Sci. Technol*. **2015**, *24*, 015025.
[24] St. Kolev, A. Bogaerts, *Plasma Sources Sci. Technol*. **2015**, *24*, 065023.
[25] G. Trenchev, St. Kolev, A. Bogaerts, *Plasma Sources Sci. Technol*. **2016**, *25*, 035014.
[26] St. Kolev, S. Sun, A. Bogaerts, Modelling of an argon gliding ''arc'' discharge, in *22nd ISPC Conf. Proc.*, 2015, *22*, P-I-2-35, 22nd ISPC, July 5-10, 2015; Antwerp, Belgium.
[27] G. Trenchev, St. Kolev, A. Bogaerts, Modelling a reverse-vortex flow gliding arc plasma reactor in 3D, in *22nd ISPC Conf. Proc.*, 2015, 22, P-I-2-71, 22nd ISPC, July 5–10, 2015; Antwerp, Belgium.
[28] J-P. Boeuf, L. L. Yang, L. C. Pitchford, *J. Phys. D: Appl. Phys*. **2013**, *46*, 015201.
[29] X. Tu, H. J. Gallon, J. C. Whitehead, Electrical and optical diagnostics of atmospheric pressure argon gliding arc plasma jet, 30th ICPIG, Belfast, UK, 28 August– 2 September, 2011, C10.
[30] Y. Korolev, O. Frants, N. Landl, A. Bolotov, V. Nekhoroshev, *Plasma Sources Sci. Technol* **2014**, *23*, 054016.
[31] W. Z. Wang, A. Berthelot, St. Kolev, X. Tu, A. Bogaerts, *Plasma Sources Sci. Technol*. **2016**, accepted for publication.
[32] V. E. Golant, A. P. Zhilinskii, I. E. Sakharov, *Fundamentals of Plasma Physics*. Wiley, New York **1980**.
[33] J. A. Bittencourt, *Fundamentals of Plasma Physics*. Springer-Verlag, New York **2004**.
[34] T. Kozák, A. Bogaerts, *Plasma Sources Sci. Technol*. **2014**, *23*, 045004.
[35] T. Kozák, A. Bogaerts, *Plasma Sources Sci. Technol*. **2015**, *24*, 015024.
[36] D. W. Hewett, C. W. Nielson, *J. Comp. Phys*. **1978**, *29*, 219–236.
[37] J. Mostaghimi, P. Proulx, M. I. Boulos, *J. Appl. Phys*. **1987**, *61*, 1753–1760.
[38] M. Touzeau, G. Gousset, C. M. Ferreira, *J. Phys. D: Appl. Phys*. **1988**, *21*, 1403–1413.
[39] L. Sansonnens, J. Haidar, J. J. Lowke, *J. Phys. D: Appl. Phys*. **2000**, *33*, 148–157.
[40] M. M. Turner, *J. App. Phys*. **1992**, *71*, 2113–2122.
[41] P. Rosenau, E. Turkel, *Phys. Scr*. **1985**, *31*, 207–209.
[42] W. Schottky, *Phys. Zeit. Bd*. **1924**, *25*, 635.
[43] P. F. Kurbatov, *Phys. Plasmas* **2013**, *20*, 043503.
[44] K. B. Persson, *Phys. Fluids* **1962**, *5*, 1625–1632.
[45] W. P. Allis, D. J. Rose, *Phys. Rev*. **1954**, *93*, 84–93.
[46] G. Wormeester, S. Pancheshnyi, A. Luque, S. Nijdam, U. Ebert, *J. Phys. D: Appl. Phys*. **2010**, *43*, 505201.
[47] Y. Kabouzi, D. B. Graves, E. Castanos-Martinez, M. Moisan, *Phys. Rev E* **2007**, *75*, 016402.
[48] R. Aerts, T. Martens, A. Bogaerts, *J. Phys. Chem. C*, **2012**, *116*, 23257–23273.
[49] L. D. Pietanza, G. Colonna, G. D'Ammando, A. Laricchiuta, M. Capitelli, *Plasma Sources Sci. Technol*. **2015**, *24*, 042002.
[50] R. Snoeckx, R. Aerts, X. Tu, A. Bogaerts, *J. Phys. Chem. C* **2013**, *117*, 4957–4970.
[51] D. C. Wilcox, *Turbulence Modeling for CFD*, 2nd edition, DCW Industries, La Cañada, CA, USA **1998**.
[52] F. H. Harlow, P. I. Nakayama, *Transport of Turbulence Energy Decay Rate*. Los Alamos Scientific Laboratory Report, LA-3854, **1968**.
[53] W. P. Jones, B. E. Launder, *Int. J. of heat Mass Tranfer* **1972**, *15*, 301–314.
[54] B. E. Launder, B. I. Sharma, *Lett. Heat Mass Trans*. **1974**, *1*, 131–138.
[55] W. M. Kays, *ASME J. Heat Trans*. **1994**, *116*, 284–295.